aerospace

MDPI

Article

Sustainable Waste Heat Utilization in Jet Engines via Integrated Guide Vane Heat Exchanger †

Gernot Burghard Hedjri-Peyfuss * and Helmut Mad

Machine Elements and Transmissions for Aviation Group, Research Unit of Machine Elements and Transmissions for Aviation, Institute of Engineering Design and Product Development, Technische Universität Wien (TU Wien), 1040 Vienna, Austria; helmut.mad@tuwien.ac.at

* Correspondence: gernot.peyfuss@tuwien.ac.at

† Presented at the Sustainable Waste Heat Utilization in Jet Engines via Integrated Guide Vane Heat Exchanger, 15th EASN Conference 2025, Madrid, Spain, 14–17 October 2025.

Abstract

High-performance geared turbofan engines generate significant heat within the planetary power gearbox. This study presents the thermal design of an integrated fan guide vane heat exchanger aimed at recovering gearbox heat losses with minimal pressure loss and converting them into useful propulsive energy via the Junkers–Meredith Effect. Hot gearbox oil is routed through hollow fan static guide vanes, enabling heat transfer to the bypass airflow while simultaneously reducing oil temperature and augmenting thrust. A comprehensive analytical framework is applied, incorporating heat transfer modeling, guide vane geometry reconstruction, lubrication flow sizing, and propulsion performance evaluation for both take-off and cruise flight conditions, using the PW1127G-JM geared turbofan as the reference engine. The results indicate that the proposed system can achieve a thrust increase of up to 6.4% at the end of take-off and deliver a thrust-specific fuel consumption reduction of up to 5.6% during take-off and approximately 2% during cruise. While sufficient heat dissipation is achieved under cruise conditions, take-off operation requires a higher transient oil temperature. Overall, this study demonstrates that integrating heat recovery into existing engine structures offers a promising pathway to enhance propulsion efficiency, reduce fuel consumption, and support more sustainable aircraft engine designs.

Keywords: guide vane heat exchanger; turbofan engine; Junkers–Meredith Effect; heat recovery; oil cooling system; thrust specific fuel consumption; sustainable waste heat utilization; planetary gearbox

Check for updates

Academic Editors: Andreas Strohmayer, Spiros Pantelakis and Gustavo Alonso-Rodrigo

Received: 30 January 2026
Revised: 3 March 2026
Accepted: 4 March 2026
Published: 9 March 2026

Copyright: © 2026 by the authors. Licensee MDPI, Basel, Switzerland. This article is an open access article distributed under the terms and conditions of the Creative Commons Attribution (CC BY) license.

1. Introduction

The European Green Deal [1] sets the objective of achieving net-zero greenhouse gas emissions in Europe by 2050, requiring substantial mitigation efforts across all major sectors, including aviation. Data from the Statista Report 2024 [2] highlight ongoing trends and projections in jet fuel consumption. The average specific jet fuel consumption of the German aircraft fleet has steadily declined over recent decades, reflecting continuous improvements in aircraft and engine efficiency. Nevertheless, the absolute fuel consumption of the aviation sector remains a critical driver of CO_2 emissions, largely due to sustained growth in air traffic demand.

The forecast estimates an average annual revenue passenger kilometers growth rate of 3.6% over the 32-year horizon, indicating that the revenue passenger kilometers may

double or even triple by 2050 compared to pre-pandemic levels in 2019, according to the International Civil Aviation Organization (ICAO) Report 2022 [3].

HXs with high thermal efficiency are becoming increasingly important for future drive systems. The cooling surface is particularly crucial for hydrogen-based electric drives [4,5].

The use of guide vanes instead of dedicated heat exchange surfaces in the bypass channel minimizes pressure loss.

Scope of This Work

High-performance planetary gearboxes in turbofan engines generate substantial heat. This thermal energy represents an underutilized opportunity for improving overall propulsion system efficiency, especially during take-off and cruise phases.

This work proposes the integration of a heat exchanger into the fan guide vanes to dissipate gearbox heat energy directly into the bypass air stream (seen in Figure 1), thereby enhancing propulsion efficiency through applying the Junkers–Meredith Effect [6] (p.6) [7], at elevated pressures due to the fan pressure ratio.

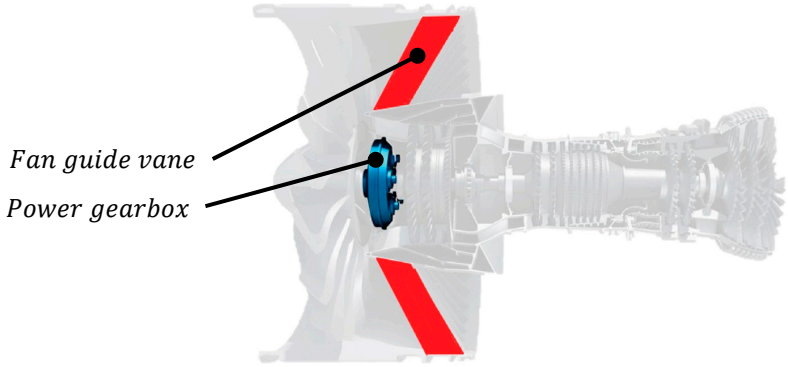


Figure 1. PW1127G-JM engine with highlighted power gearbox (blue) and fan guide vanes (red) [8].

2. Objective

The aim of this work is the thermal and structural design of a guide vane heat exchanger to recover and utilize gearbox thermal energy. The concept involves channeling oil through hollow fan guide vanes to dissipate heat to the bypass airflow, simultaneously serving as a thermal sink of the oil circuit and enabling thrust enhancement. Particular focus is placed on the flight phases take-off, due to the high power demand of this phase, and cruise, due to this phase being the majority of the flight time.

3. Materials and Methods

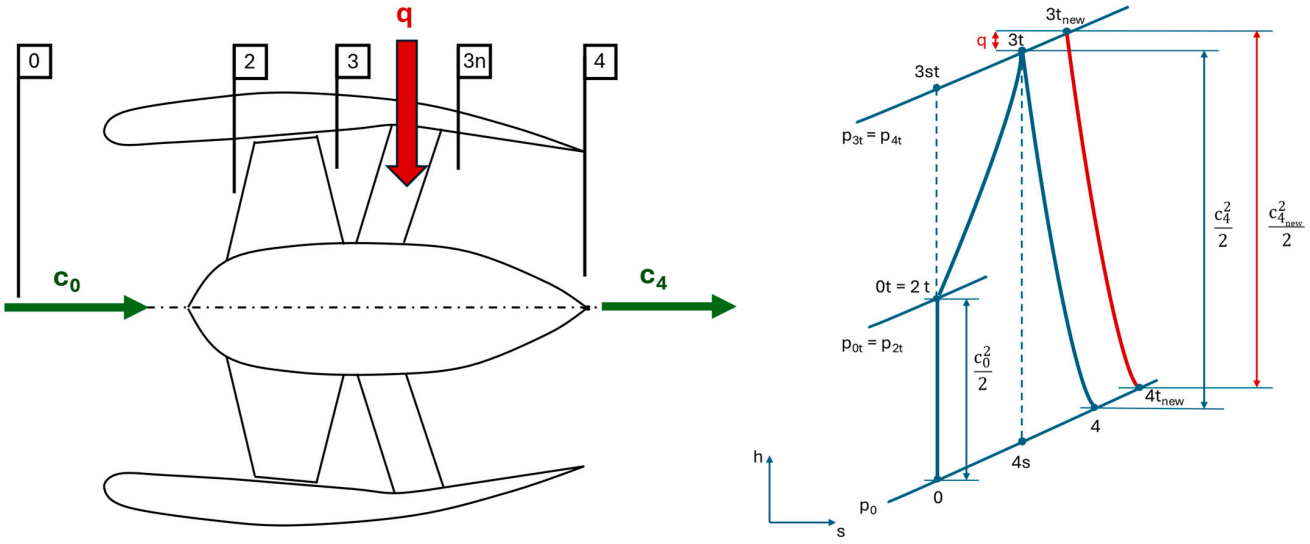
This section outlines the analytical framework, engine reference configuration, and heat transfer models applied to design and evaluate the integrated fan guide vane heat exchanger, including oil supply sizing and thrust augmentation methodology.

3.1. Junkers–Meredith Effect

When the hot coolant passes through the aircraft radiator, it releases heat to the surrounding air, which warms up, expands, and accelerates as it exits through a narrow outlet. This accelerated airflow produces a jet-like thrust that partially offsets the radiator's aerodynamic drag.

A simple propulsor model (shown in Figure 2a) consists of a lossless inlet duct (0–2), a rotating rotor fan blade row (2–3), and a stator guide vane row (3–3n) in a housing. By applying thermal energy q between sections 3 and 3n in the guide vane row, the air velocity at the nozzle outlet c_4 can be increased. Figure 2b shows the increase effect with c_{4new} due to q in an h-s-diagram. The increase effect based on the divergence of the isobaric

pressure lines induced by the temperature rise signifies an increase in specific enthalpy, which directly leads to an increment in the nozzle exit velocity and, therefore, thrust.



(**a**) (**b**)

Figure 2. (**a**) Simple propulsor model with inter-heating by the gearbox oil. (**b**) Simplified h-s-diagram of a simple propulsor model to illustrate the impact of the Junkers–Meredith Effect.

The heat exchanger is assumed to operate under isobaric conditions with negligible total-pressure losses. The temperature increase ΔT_A of the air mass flow $\dot{m}_A$ occurs due to the hot gear oil mass flow $\dot{m}_0$ and is ideally without losses. It can be explained using Equation (1), with the use of the specific isobar air heat capacity $c_{p,A}$, and is visible in Figure 2b.

$$\dot{m}_0 \cdot q = \Delta T_A \cdot \dot{m}_A \cdot c_{p,A} = (T_{3,n} - T_3) \cdot \dot{m}_A \cdot c_{p,A} \quad (1)$$

Thrust Gain

The derivation for Equations (2)–(7) can be found in Bayindir 2025 [9]. In the case of ideal, isentropic compression at the fan and isentropic expansion at the nozzle, where the isentropic efficiencies of the fan and nozzle $\eta_{S,Fan} = \eta_{S,Nozzle} = 1$, this allows $T_4 = T_0$ to apply. The fan pressure ratio (FPR) is expressed by π_F. In this case, the expression for the jet velocity c_4 is simplified to

$$c_4 = \sqrt{\frac{2 \cdot \varkappa \cdot R}{\varkappa - 1} \cdot T_0 \cdot \left[\pi_F^{\frac{\varkappa - 1}{\varkappa}} \cdot \left(1 + \frac{\varkappa - 1}{2} \cdot Ma_0^2 \right) - 1 \right]} \quad (2)$$

Assuming an ideal isentropic expansion in the thrust nozzle, the modified jet velocity $c_{4,new}$ can be calculated using the heat exchanger (HX) increased total temperature $T_{3,n}$. The description for $T_{3,n}$ can be found under Equation (3).

$$c_{4,new} = \sqrt{\frac{2 \cdot \varkappa \cdot R}{\varkappa - 1} \cdot T_{3,n} \cdot \left[1 - \frac{1}{\pi_F^{\frac{\varkappa - 1}{\varkappa}} \cdot \left(1 + \frac{\varkappa - 1}{2} \cdot Ma_0^2 \right)} \right]} \quad (3)$$

The thrust generated by the fan can be simply expressed in the propulsion model as the forces F_N and $F_{N,HX}$. It can be determined using the jet velocity c_4, the air speed c_0 and

the air mass flow $\dot{m}_A$. This consideration only addresses the difference in speed, not the difference in pressure.

$$F_N = (c_4 - c_0) \cdot \dot{m}_A \tag{4}$$

$$F_{N,HX} = (c_{4,new} - c_0) \cdot \dot{m}_A \tag{5}$$

The thrust F_N describes the ideal achievable thrust generated by the fan in the propulsion model. The thrust $F_{N,HX}$ describes the ideal achievable thrust generated by the fan and by additional heating in the propulsion model. The thrust obtained by the additional heating is described by ΔF_N and is defined as follows:

$$\Delta F_N = F_{N,HX} - F_N \tag{6}$$

The new improved thrust specific fuel consumption $\mathrm{SFC_{T,new}}$ can, therefore, be calculated using Equation (7):

$$\mathrm{SFC_{T,new}} = \frac{m_B}{F_N + \Delta F_N} \tag{7}$$

The thrust increase ε_F can be obtained using Equation (8):

$$\varepsilon_F = \frac{\Delta F_N}{F_N} \tag{8}$$

As a result, the Junkers–Meredith Effect converts heat from the cooling system into additional propulsion, improving overall efficiency due to the ramjet effect. The results with the description can be found in Section 4.2.

3.2. Selection of the Engine

The PW-1127G-JM engine was selected as the reference configuration because many parameters of the planetary fan power gearbox for this turbofan are already known from studies [9–11], and with a total of 48 fan guide vanes, the design features a high vane count and, therefore, a high surface area for the heat exchanger, as depicted in Figure 3.

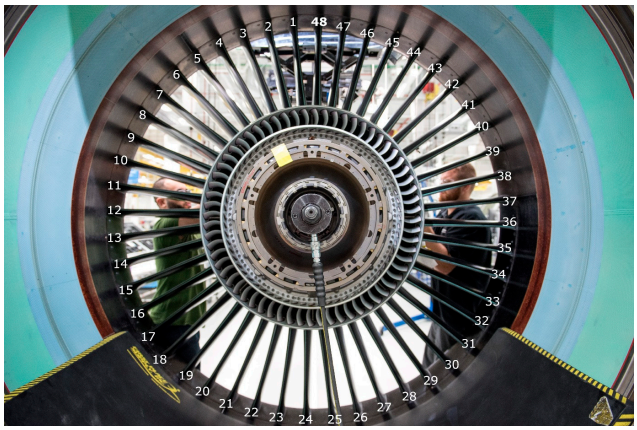


Figure 3. Fan outlet guide vane count of a PW1100G-JM, with numbered fan guide vanes [12].

3.3. Performance Characteristics

The thesis from Peyfuß 2025 [10] replicates fan performance characteristics, with a Gasturb [13] simulation of the PW 1127G-JM for take-off and cruise flight phases. The cruise flight phase was determined by the thrust specifications from the EASA certification documents [14], and the take-off flight phase was designated as off-design. The total fan power is used for the calculation and can be found in Table 1.

Table 1. Parametric study constant input parameters for take-off and cruise flight phases, calculated with Gasturb.

Parameter	Take-Off	Cruise
Thrust F_N [kN]	120.43	19.12
Fan power P_{Fan} [MW]	15.9661	6.2537
SFC_T $[\frac{g}{kN \cdot s}]$	6.9875	13.6134

The change in efficiency can be taken from the ASME Turbo Expo 2020 study [11], which analyzed the power loss of the power gearbox in the geared turbofan PW1100G (P&W Engine) of an A320neo with a modeled thrust design point of $F_{N,ASME}$ = 112.5 kN by take-off and compared it with the Rolls-Royce Ultrafan (Scaled Engine) throughout all phases of flight, visible in Figure 4. This value of thrust is lower than that of the PW1127G-JM, which delivers a thrust of F_N = 120.43 kN for the take-off flight phase. However, the values of the thrusts $F_{N,ASME}$ and F_N are very close to each other, so the efficiency η_G of the power gearbox is very comparable. The comparison between PW1100G and RR Ultrafan was chosen due to their large bypass ratios.

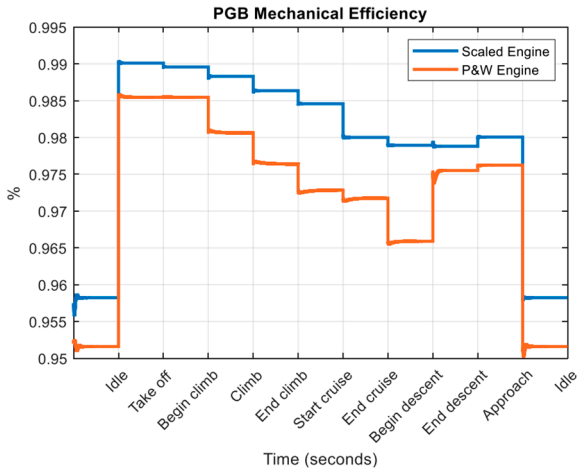


Figure 4. Efficiency of the power gearbox of a PW 1100G (orange) and a RR Ultrafan (blue) throughout all phases of flight [11] (p.5).

The efficiency η_G for take-off and cruise is extracted from Figure 4, whereby an average value of *Start cruise* and *End cruise* was calculated for the cruise flight phase and can be seen in Table 2. The power loss of the planetary gear can be determined with the help of the efficiency values, as shown in Equation (9):

$$P_V = P_{FAN} \cdot (1 - \eta_G) \tag{9}$$

Table 2. Performance efficiency parameters for take-off and cruise flight phases.

Parameter	Take-Off	Cruise
Gearbox efficiency η_G [-]	0.9855	0.9725
Power loss P_V [kW]	231,508	171,977

The power loss occurring due to Equation (9) can be seen in Table 2.

The pressure loss in the HX is neglected for this part of the calculation, allowing investigation of the upper efficiency limit of the process.

3.4. Fan Guide Vanes Heat Exchanger Design

For the temperature considerations in the initial design, a cross-flow heat exchanger was used for simplicity, which must dissipate the total power loss of the power gearbox. This results in two boundary conditions:

- The heat capacity flow must be sufficient to dissipate the heat flow within the specified temperatures.
- The inlet temperature of the hot oil to the heat exchanger should be $T_{O,in} = 150\ ^\circ\text{C}$ and at the outlet of the heat exchanger should be $T_{O,out} = 110\ ^\circ\text{C}$.
- It is assumed that the air is always dry.
- No contamination and continuous degassing of the oil.
- For the initial design, only the heat conduction through the guide vane and the heat flows of oil and air are taken into account, without taking cover into account.
- Heat radiation is neglected due to its significantly lower importance compared to heat flows.

3.4.1. Parameters for Heat Exchanger and Thrust Gain Calculation

For the design of the heat exchanger and to calculate the airspeed and thrust, the required values are taken from Position 0 and 13 of the gas turbine calculation from the thesis by Peyfuß 2025 [10] and listed in Table 3. Figure 5 indicates Position 0 in front of the air intake, Position 2 in front of the fan and Position 13 near the fan guide vane in the bypass channel.

Table 3. Input parameters for air at take-off and cruise flight phases [10] (p.133–134).

Parameter	Take-Off	Cruise
Air total temperature $T_{A,0}$ [K]	298.15 (25 °C)	219.06 (−54.09 °C)
Air velocity $c_{A,0}$ $[\frac{\text{km}}{\text{h}}]$	0	840
Air Mach number $Ma_{A,0}$ [-]	0	0.78
Air total temperature $T_{A,13}$ [K]	331.63 (58.48 °C)	275.60 (2.45 °C)
Air velocity $c_{A,13}$ $[\frac{\text{m}}{\text{s}}]$	142.172	146.833
Air mass flow $\dot{m}_{A,13}$ $[\frac{\text{kg}}{\text{s}}]$	449.153	198.269
Density of air $\rho_{A,13}$ $[\frac{\text{kg}}{\text{m}^3}]$	1.38561	0.59349
Kinematic air viscosity $\nu_{A,13}$ $[\frac{\text{mm}^2}{\text{s}}]$	13.584	13.678
Specific isobar air heat capacity $c_{pA,13}$ $[\frac{\text{J}}{\text{kg}\cdot\text{K}}]$	1007.55	1004.21
Thermal air conductivity $\lambda_{A,13}$ $[\frac{\text{W}}{\text{mK}}]$	0.028457	0.024405
Fan pressure ratio π_F [-]	1.40606	1.446
Air temperature increase ΔT_A [K]	0.512	0.864

Position 13 of the turbofan model seen in Figure 5 is equivalent to Position 3 of the simple propulsor model seen in Figure 2a. The analysis in the Gasturb model is based on energy equations similar to the simple propulsion model in Figure 2a, without taking velocity vectors of the fan or guide vanes into account. This means that Position 3 is equal to 3n if no thermal energy q is supplied. Only when the thermal energy q is introduced does a difference between Position 3 and 3n arise. Position 0 in the Gasturb model is the same as in the propulsor model.

At the end of the take-off flight phase, it can be assumed that the Mach number must have reached $Ma_{A,0} = 0.25$ for the aircraft to take off at sea level [15].

The gas constant $R = 287.05\ \frac{J}{kg\cdot K}$ [10] and the isentropic exponent $\varkappa = 1.4$ [16] remain constant in both flight phases; both parameters are for dry air.

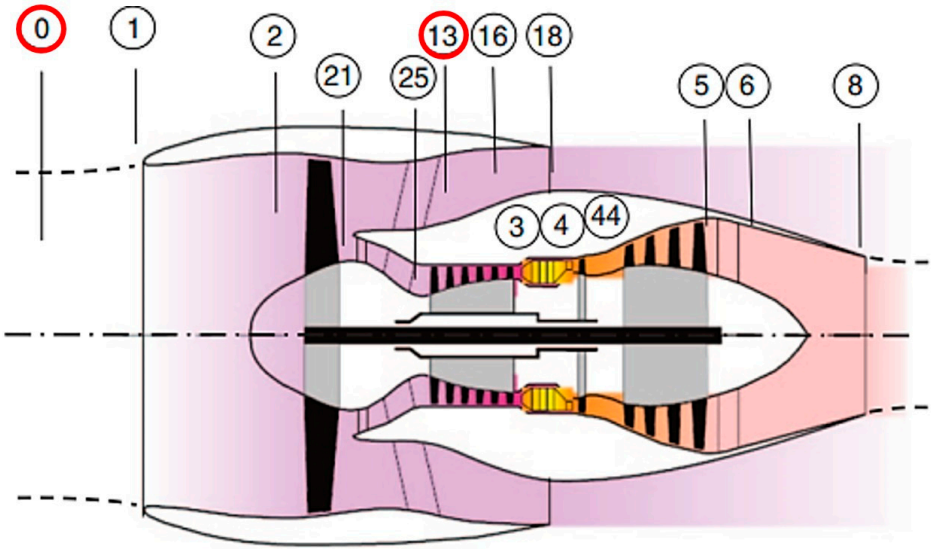


Figure 5. Gasturb model of a turbofan with design points; the important ones are circled in red [13].

The temperature increase ΔT_A is explained in Equation (1). Ideally, the power loss P_V can be equated with $\dot{m}_0 \cdot q$, which gives us Equation (10):

$$\Delta T_A = \frac{P_V}{\dot{m}_A \, c_{p,A}} \tag{10}$$

The slight increase in air temperature is due to the very high air mass flow, as shown in Table 3.

The parameters for the gearbox oil can be found in Liebherr 2007 [17] and are listed in Table 4; these parameters are required for the thermal calculations. Only the thermal conductivity λ_O had to be approximated using lubrication machine oil [18]. The calculation was based on the properties of AERO SHELL TURBINE OIL 500 [19], which is suitable for the specified operating temperature and was also used in Liebherr 2007 [17]. For the calculation of further heat transfer, the average oil temperature $T_{O,m}$ is required and is described in Equation (11):

$$T_{O,m} = \frac{T_{O,in} + T_{O,out}}{2} \tag{11}$$

Table 4. Input parameters for oil [17], (p. 78) [18].

Parameter	Value
Gearbox oil inlet temperature $T_{O,in}$ [K]	383.15 (110 °C)
Gearbox oil outlet temperature $T_{O,out}$ [K]	423.15 (150 °C)
Average gearbox temperature $T_{O,m}$ [K]	403.15 (130 °C)
Kinematic oil viscosity at $T_{O,m}$ $\nu_{O,m}[\frac{mm^2}{s}]$	3.6
Kinematic oil viscosity at $T_{O,in}$ ν_O $[\frac{mm^2}{s}]$	5
Specific heat capacity of oil at $T_{O,m}$ $cp_{O,m}$ $[\frac{J}{kg \cdot K}]$	1899
Specific heat capacity of oil at $T_{O,in}$ cp_O $[\frac{J}{kg \cdot K}]$	1816
Density of oil at $T_{O,m}$ $\rho_{O,m}$ $[\frac{kg}{m^3}]$	885
Density of oil at $T_{O,in}$ ρ_O $[\frac{kg}{m^3}]$	905
Thermal oil conductivity λ_O $[\frac{W}{mK}]$	0.126

To maintain high thermal conductivity, TiAl4V (Titan Grade5) alloy is used for the guide vane. A protective strip of titanium is already being used at the front tip of the guide vane [10]. The required parameters are listed in Table 5 [20].

Table 5. Input parameters for guide vane material TiAl4V alloy [20].

Parameter	Value
Density of TiAl4V ρ_{Ti} $[\frac{kg}{m^3}]$	4430
Thermal TiAl4V conductivity λ_{Ti} $[\frac{W}{mK}]$	7.1

All the input parameters for Tables 4–6 are required for the thermal calculations in Section 3.4.5. "Heat Transfer Models".

Table 6. Input parameters for guide vane geometry [10] (p.84–85).

Parameter	Value
Cord length s [mm]	163
Guide vane length L [mm]	590
Wall thickness δ_{Ti} [mm]	2
Average upper height $y_{U,m}$ [-]	0.053
Average lower height $y_{L,m}$ [-]	0.0055
Average oil channel height $h_{O,m}$ [mm]	3.74

3.4.2. 3D Reconstruction

The proportions of the guide vane could be replicated using the specified fan diameter. Only the sweep angle was taken into account. The contour of the guide vane was approximated with a NACA 6409, as no precise details of the profile are available and sufficient for a basic interpretation. The NACA 6409 thus has a profile camber of 6%, a camber reserve of 40% and a profile thickness of 9% in relation to cord length s, as shown in Figure 6.

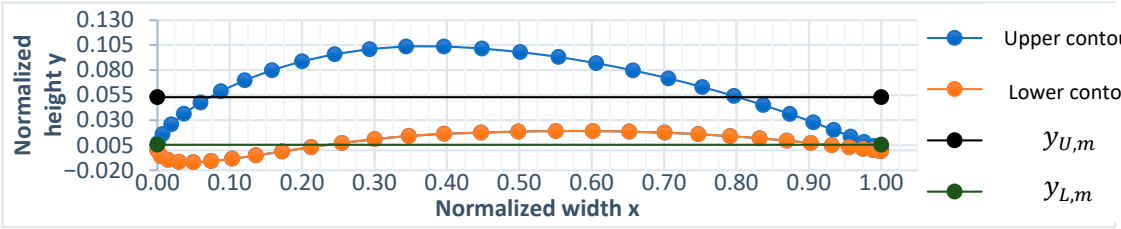


Figure 6. NACA 6409 air foil build up the contour with reference points and average heights y_m limits.

In Figure 6, the average heights of the y coordinates for the upper NACA contour in blue and the lower NACA contour in orange are described by the upper limit $y_{U,m}$ and lower limit $y_{L,m}$ from 0 to 1 of the normalized width. By subtracting the lower part $y_{L,m}$ from the upper part $y_{U,m}$, the average height of the oil channel $h_{O,m}$ can be determined while taking into account the wall thickness δ_{Ti} and scaling with the cord length s, as shown in Equation (12):

$$h_{O,m} = \left(y_{U,m} - y_{L,m}\right) \cdot s - 2 \cdot \delta_{Ti} \quad (12)$$

The NACA 6409 profile is used for further design to ensure a sufficiently large cross-section for the oil. In the initial design, other angles and twists are neglected, as these are minimal based on the Figures in [10] (p. 89).

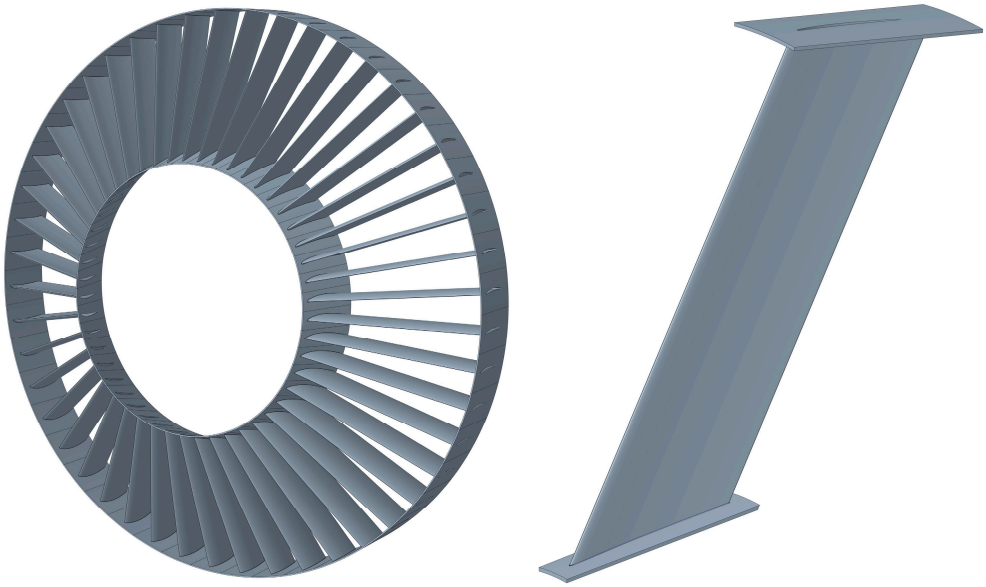
The exact value of the angle of attack is required for precise positioning or profile selection. This can only be determined using simulations or real speed measurements in order to form the speed triangles. A more detailed examination of the air velocity and pressures across the profile for different flight phases only becomes meaningful once the fan and blade geometries are known.

A simplified fan guide vane row is reconstructed considering oil channels through the guide vane, as shown in Figure 7. For the design point, the wall thickness δ_{Ti} of the guide vane is assumed to be 2 mm. The oil channel has a radius of 2 mm in the front and rear areas of the guide vane.



Figure 7. Redesigned cross-section of the NACA 6409 guide vane with integrated oil channel.

The entire guide vane row can be seen in Figure 8a, and a single segment of this row is visible in Figure 8b. The dimensions for the construction are taken from Peyfuß 2025 [10] and are listed in Table 6.



(**a**) (**b**)

Figure 8. (**a**) Redesigned fan guide vane row; (**b**) single guide vane segment.

By choosing TiAl4V alloy as the material instead of the compound solution with a titanium protective strip currently in use, the additional fastening clamps, clamping screws and protective strips can be eliminated. In addition, the outer and inner guide vane cover can be integrated into the guide vane. This results in a complete blade module consisting of a single component.

3.4.3. HX Surfaces

Heat transfer models and logarithmic mean temperature difference are used to determine effective heat transfer through surface area. The heat transfer surface area was divided as shown in Figure 9.

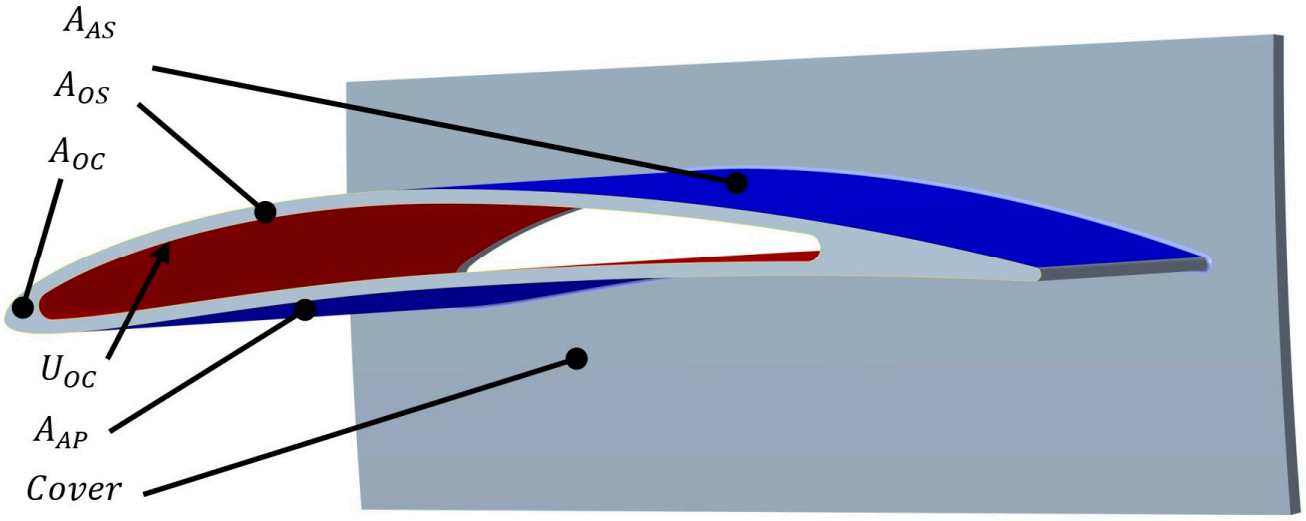


Figure 9. Isometric cross-section of the redesigned guide vane, with colored HX surfaces and circumference and cover endplate.

To simplify the system, only the guide vanes are used for HX calculations, as can be seen in Figure 9. The outer cover surfaces are not taken into account for heat transfer, which leads to a conservative result. On the air side, only those parts of the suction and pressure sides that have translational air velocity across the surface are used (shown in blue). The oil channel is located inside the guide vanes (highlighted in red in Figure 9). The entire circumferential surface is used for heat transfer, except for the start and end regions where the cover wall thickness is present. All parameters mentioned in Figure 9 can be found in Table 7.

Table 7. Input parameters for guide vane surfaces and circumference.

Parameter	Value
Air HX surface suction side $A_{A,S}$ [mm^2]	93,831.95
Air HX surface pressure side $A_{A,P}$ [mm^2]	90,646.79
HX surface oil channel side $A_{O,S}$ [mm^2]	142,552.9
Oil channel cross − sec tion A_{OC} [mm^2]	4016.04
Oil circumference U_{OC} [mm]	309.99
Equivalent channel diameter $d_{O,m}$ [mm]	51.82

The general formula for a comparable equivalent oil channel diameter $d_{O,m}$ is calculated, using Equation (13), with the help of the cross-sectional area A_{OC} and the circumference U_{OC} of the oil channel from Table 7:

$$d_{O,m} = \frac{4 \cdot A_{OC}}{U_{OC}} \tag{13}$$

3.4.4. Oil Flow Design

The design of the lubrication system starts with the determination of the oil flow rate required to remove the heat losses. This calculation is based on prescribed temperature limits. The values of $T_{O,out}$ and $T_{O,in}$ can be found in Table 4.

$$\Delta T_{O,m} = T_{O,out} - T_{O,in} \tag{14}$$

$$\dot{V}_{O,m} = \frac{P_V}{\rho_O \cdot c_{pO} \cdot \Delta T_{O,m}} \tag{15}$$

The volumetric oil flow $\dot{V}_{O,m}$ can be determined using Equation (15) [17] (p.67) and can be expressed in terms of mass flow rate $\dot{m}_O$ (Equation (16)) and velocity c_O (Equation (17)):

$$\dot{m}_O = A_{O,C} \cdot \rho_O \cdot c_O \tag{16}$$

$$c_O = \frac{\dot{m}_O}{A_{O,C} \cdot \rho_O} = \frac{\dot{V}_O}{A_{O,C}} \tag{17}$$

The density of the oil ρ_O for Table 8 can be found in Table 4.

Table 8. Required oil parameters.

Parameter	Take-Off	Cruise
Required volumetric oil flow rate $\dot{V}_{O,r}$ $[\frac{l}{min}]$	212.2	156.96
Required mass oil flow rate $\dot{m}_{O,r}$ $[\frac{kg}{s}]$	3.20	2.37
Required oil flow velocity $c_{O,r}$ $[\frac{m}{s}]$	0.88	0.65

This results in a volume flow that is very similar to that in the Liebherr final report, with an oil delivery rate designed at 180 L/min for a max gearbox power loss of 217.8 kW [17] (p. 69).

To account for uncertainties in the system design, a safety margin is applied to the oil velocity. Furthermore, it can be assumed that the engine speed remains approximately constant during the cruise and take-off phases of the flight because the oil pump's flow rate depends on the speed of the drive. This results in a design velocity of

$$c_O = 1 \text{ m/s} \tag{18}$$

which represents a commonly accepted value in lubrication system design. Based on this velocity, the adjusted oil mass flow rate is calculated and shown in Table 9.

Table 9. Chosen oil parameters for take-off and cruise flight phases.

Parameter	Value
Chosen volumetric oil flow rate $\dot{V}_O$ $[\frac{l}{min}]$	240.96
Chosen mass oil flow rate $\dot{m}_O$ $[\frac{kg}{s}]$	3.63

3.4.5. Heat Transfer Models

The velocity and pressure distributions along the guide vane profile differ between the suction and pressure sides and, additionally, may vary with the flight phase, as can be seen in Durmus et al. 2023 [21] (p. 9).

Since no data on the guide vane geometry is available, a simplified approach using an average velocity across both sides of the guide vane profile can be used. Also, the suction and pressure sides of the guide vane are approximated for the HX calculation by straight plates with a constant average velocity. This assumption is justified by a simplified approximation, since the velocity is zero at the stagnation point at the leading edge of the guide vane. An HX model, as shown in Figure 10, is constructed for the suction and pressure sides.

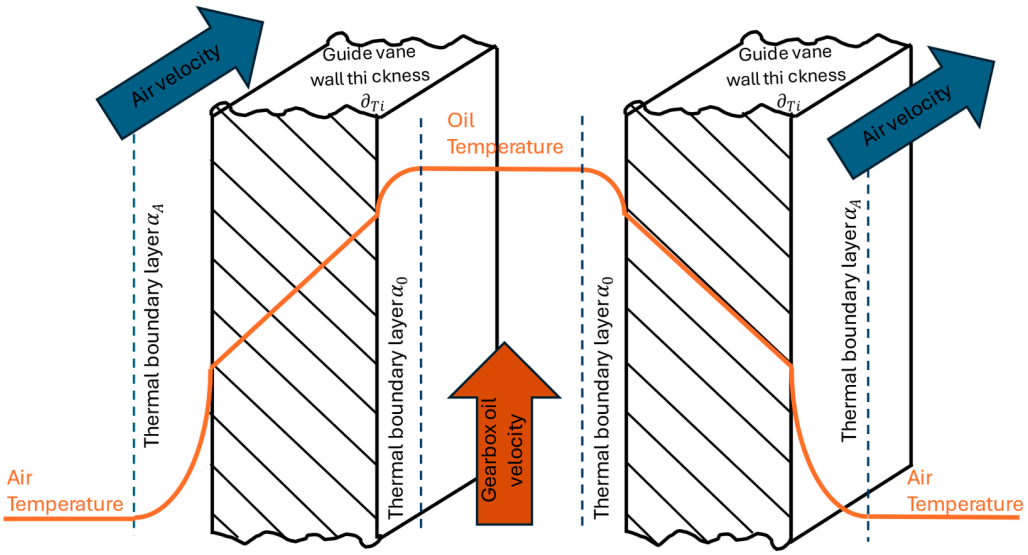


Figure 10. Heat transfer model of a single guide vane, with simplified oil channel geometry.

Since both sides have the same wall thickness and the air velocity and heat transfer coefficient are averaged, the pressure and suction sides of the guide vane can be simplified to a single heat transfer with both surfaces. The thermal boundary layers further impede heat transfer through the wall thickness of the titanium blade, as seen in Figure 11.

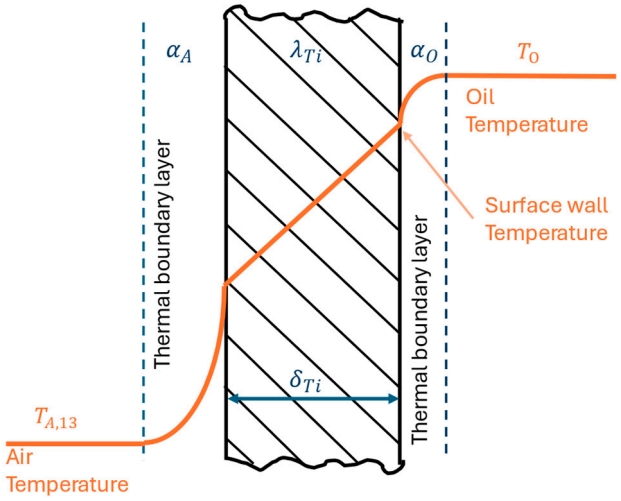


Figure 11. Improved simplified heat transfer model of a plain wall.

Equations (19)–(35), used to calculate heat transfer, are adopted from the VDI Wärmeatlas [22]. In order to determine the necessary surface area for the heat exchanger, the heat conduction through the guide vane must be determined using the average heat transfer coefficient k through a static plate. This can be calculated using Equation (19):

$$k = \left(\frac{1}{\alpha_A} + \frac{\delta_{Ti}}{\lambda_{Ti}} + \frac{1}{\alpha_O} \right)^{-1} \tag{19}$$

Since the thermal conductivity λ_{Ti} and wall thickness δ_{Ti} of TiAl4V alloy are already given in Tables 6 and 7, only the heat transfer coefficient of the air α_A and the gearbox oil α_O still need to be determined.

$$\alpha = \frac{Nu_m \cdot \lambda_F}{L_c} \tag{20}$$

Here, λ_F represents the thermal conductivity of the fluid, and L_c represents the hydraulic characteristic length, which corresponds to the chord length s of the guide vane for α_A. For the internal flow α_O in the cross-sectional area, the characteristic length L_c can be approximated by twice the average height h_m of the guide vane channel when viewed from a plane slit perspective. The oil channel can also be viewed as a flow-through pipe, which changes the characteristic hydraulic length to the channel diameter $d_{O,m}$.

In order to determine the mean Nusselt number Nu_m, the Reynolds number Re and Prandtl number Pr must be calculated to ensure that the flow is turbulent and within the valid range.

$$Re = \frac{c \cdot L_c}{\nu} \tag{21}$$

where ν describes the kinematic viscosity and c describes the velocity over the area.

$$Pr = \frac{\nu \cdot c_p \cdot \rho}{\lambda_F} \tag{22}$$

To determine α_A, the guide vane is considered to be a longitudinally flowed plate. It is not permissible to consider it as a transversely flowed single row of tubes, as the Reynolds number would then be too high. However, the formula for the turbulent and laminar Nusselt numbers is the same in both cases. Equation (23) can be found at [22] (p. 806).

$$Nu_{m,A} = \sqrt{Nu_{L,A}^2 + Nu_{T,A}^2} \cdot K \tag{23}$$

$$K_A = \left(\frac{T_M}{T_W}\right)^{0.12} \tag{24}$$

The K-factor for air K_A [22] (p.807) can be assumed to be equal to 1 due to the very high air mass flow and the resulting very small difference between T_M and T_W. It should be taken into account in iterative calculations. The laminar Nusselt number $Nu_{L,A}$ can be found at [22] (p.805), and the turbulent part $Nu_{T,A}$ can be found at [22] (p.806).

$$Nu_{L,A} = 0.664 \cdot \sqrt{Re} \cdot \sqrt[3]{Pr} \tag{25}$$

$$Nu_{T,A} = \frac{0.037 \cdot Re^{0.8} \cdot Pr}{1 + 2.443 \cdot Re^{-0.1} \cdot \left(Pr^{\frac{2}{3}} - 1\right)} \tag{26}$$

The validity range of a longitudinally flowed plate for $Nu_{m,A}$ is $10^1 < Re < 10^7$ and $0.5 < Pr < 2000$ [22] (p.806). These limits can be compiled and are shown in Table 10.

Table 10. Intermediate values for air heat transfer in take-off and cruise flight phases.

Parameter	Take-Off	Cruise
Reynolds number for air Re_A [−]	1,705,980	1,749,801
Prandtl number for air Pr_A [−]	0.6664	0.3340
Nusselt number for air $Nu_{m,A}$ [−]	2868.53	1848.44
Heat transfer coefficient of air α_A $[\frac{W}{m^2K}]$	500.80	276.76

During cruise conditions, the Prandtl number lies outside the applicable validity range. Therefore, an equation must be used that is still valid for small Prandtl numbers.

Equation (27) [23] (p.344) applies to the entire range of Pr for laminar flow over a straight surface with constant flux surface:

$$Nu_{L,A,C} = \frac{0.696 \cdot Re^{1/2} \cdot Pr^{1/3}}{\left[1 + (0.0205/Pr)^{2/3}\right]^{1/4}} \tag{27}$$

No equation could be found for the turbulent portion of the Nusselt number $Nu_{T,A,C}$ that would allow Prandtl numbers smaller than 0.5. To keep the error small, the previously calculated turbulent portion is reduced by the ratio of the laminar portion $Nu_{L,A,C}/Nu_{L,A}$. The values for the air heat transfer can be found in Table 11.

Table 11. Intermediate values for air heat transfer in the cruise flight phase for entire range of Pr.

Parameter	Cruise
Lamina Nusselt number for air $Nu_{L,A,C}$ $[-]$	616.10
Ratio laminar portion $Nu_{L,A,C}/Nu_{L,A}$ $[-]$	1.01098
Turbulent Nusselt number for air $Nu_{L,A,T}$ $[-]$	1764.25
Nusselt number for air $Nu_{m,A,C}$ $[-]$	1868.73
Heat transfer coefficient of air $\alpha_{A,C}$ $[\frac{W}{m^2K}]$	279.79

The deviation of the heat transfer coefficient $\alpha_{A,C}$ for Prandtl numbers greater than 0.5 from that applicable to the entire Prandtl range is very small. This is because the calculated Prandtl number is just below the limit. As can be seen from the Re, the turbulent component predominates strongly. Therefore, the laminar component cannot be used as a sufficient reference. For this reason, the values in Table 11 are used for further calculations, even if this results in a slight error, which is acceptable for the basic design.

Since the oil channel is very narrow and elongated and hardly any heat exchange can take place at the stagnation point, a flat gap can be considered to determine $\alpha_{O,I}$. For the correct choice of the Nusselt number, it must be taken into account as a boundary condition that both sides of the gap have the same wall temperature, as can be seen in Figure 10. This changes the formulas for the Nusselt number to [22] (p. 800)

$$Nu_{1,O,I} = 7.541 \tag{28}$$

$$Nu_{2,O,I} = 1.841 \cdot \sqrt[3]{Re \cdot Pr \cdot \frac{2 \cdot h_m}{L}} \tag{29}$$

$$Nu_{m,O,I} = \left(Nu_{1,O}^3 + Nu_{2,O}^3\right)^{\frac{1}{3}} \tag{30}$$

In Equation (29), the parameter L is the flow length of the oil in the guide vane [22] (p.800).

The average oil channel height h_m can be found in Table 6. The validity range of a plate for $Nu_{m,O,I}$ is $Re \leq 2200$ [22] (p. 799).

By changing the approach to a flow-through pipe, the Nusselt number can be calculated for fully developed turbulent flow. The average Nusselt number $Nu_{m,O,II}$ [22] (p. 788) for Tubes is now defined as

$$Nu_{m,O,II} = \frac{\frac{(1.8 \cdot \lg(\mathrm{Re}) - 1.5)^{-2}}{8} \cdot Re \cdot Pr}{1 + 12.7 \cdot (Pr^{\frac{2}{3}} - 1) \cdot \sqrt{\frac{(1.8 \cdot \lg(\mathrm{Re}) - 1.5)^{-2}}{8}}} \cdot \left(1 + \left(\frac{d_{O,m}}{L}\right)^{\frac{2}{3}}\right) \tag{31}$$

The validity range of a flow-through pipe for $Nu_{m,O,II}$ is $10^4 \leq Re \leq 10^6$, besides that $0.1 \leq Pr \leq 1000$ and $\frac{d_{O,m}}{L} \leq 1$ [22] (p. 788). These limits can be compiled and are shown in Table 12.

Table 12. Intermediate values for oil heat transfer, considered as a plate I or as a pipe II.

Parameter	Value
Reynolds number for oil by $T_{O,m}$ $Re_{O,m,I}[-]$	2078
Prandtl number for oil by $T_{O,m}$ $Pr_{O,m,I}[-]$	48
Nusselt number for oil $Nu_{m,O,I}[-]$	20.26
Heat transfer coefficient of oil $\alpha_{O,I}[\frac{W}{m^2 K}]$	682.56
Reynolds number for oil by $T_{O,m}$ $Re_{O,m,II}[-]$	14,394
Prandtl number for oil by $T_{O,m}$ $Pr_{O,m,II}[-]$	48
Nusselt number for oil $Nu_{m,O,II}[-]$	284.25
Heat transfer coefficient of oil $\alpha_{O,II}[\frac{W}{m^2 K}]$	691.15

Both methods provide very nearly similar results for α_O, so calculations are continued using the $\alpha_{O,I}$ value, as shown in Figure 11.

The average heat transfer coefficient k can now be calculated with Equation (19).

The required heat exchange area A_{HX} is calculated using the heat flow $\dot{Q}$, which corresponds as gearbox power loss P_V, as well as the heat transfer coefficient k and logarithmic mean temperature difference $\Delta T_{m,\log}$ (Equation (33) until (36)). By equating P_V with $\dot{Q}$, the previously selected volume flow of the oil is no longer included and can be seen in Equation (32):

$$A_{HX} = \frac{\dot{Q}}{k \cdot \Delta T_{m,\log}} = \frac{P_V}{k \cdot \Delta T_{m,\log}} \tag{32}$$

In cross-flow direct-current heat exchangers, the greatest temperature difference occurs at the beginning, and the smallest occurs at the end, similar to a direct-flow heat exchanger.

$$\Delta T_{m,\log} = \frac{\Delta T_{max} - \Delta T_{min}}{\ln\left(\frac{\Delta T_{max}}{\Delta T_{min}}\right)} \tag{33}$$

$$\Delta T_{max} = T_{O,out} - T_{A,3} \tag{34}$$

$$\Delta T_{min} = T_{O,in} - T_{A,3n} \tag{35}$$

$$T_{A,3n} = T_{A,3} + \Delta T_A \tag{36}$$

This allows the required heat exchange area $A_{HX,min}$ for the take-off and cruise flight phases to be determined, which can be seen in Table 13.

Table 13. Values of the heat transfer model as well as requirements and limits for take-off and cruise.

Parameter	Take-Off	Cruise
Mean heat transfer coefficient k $[\frac{W}{m^2 K}]$	267.125	186.567
Log. mean temperature difference $\Delta T_{m,\log}$ [K]	69.303	126.018
Required heat exchange surface $A_{HX,min}$ $[m^2]$	12.505	7.315
Maximum transferable power loss $P_{V,max}$ [kW]	163.928	208.188
Efficiency of the heat exchanger ε_{HX} [-]	0.436	0.271

The efficiency ε_{HX} of the HX is defined as shown in Equation (37) and can be found in Table 13 [22] (p. 45).

$$\varepsilon_{HX} = \frac{\dot{Q}}{\dot{Q}_{max}} = \frac{P_V}{\dot{m}_{min} \cdot c_{p,min} \cdot (T_{O,out} - T_{A,3})} \tag{37}$$

The low heat capacity in both flight phases is that of the gear oil. The maximum power $P_{V,max}$ that can be dissipated via the guide vane is lower during the take-off phase than the existing power P_V, which also explains the much larger required heat exchanger surface $A_{HX,min}$.

For both flight phases, the oil volume flow $\dot{V}_{\mathrm{O}}$ is reduced from 240.96 L/min to the required volumetric oil flow rate $\dot{V}_{\mathrm{O,r}}$ (Table 8). For the take-off flight phase, $\dot{V}_{\mathrm{O,\,r,\,T}} = 212.2$ L/min, and for the cruise flight phase, it is reduced to $\dot{V}_{\mathrm{O,\,r,\,C}} = 156.96$ L/min, as otherwise the equation system would be overdetermined.

The temperature curves for both flight phases, take-off (solid lines) and cruise (dashed lines), for the values specified in Table 13 can be seen in Figure 12.

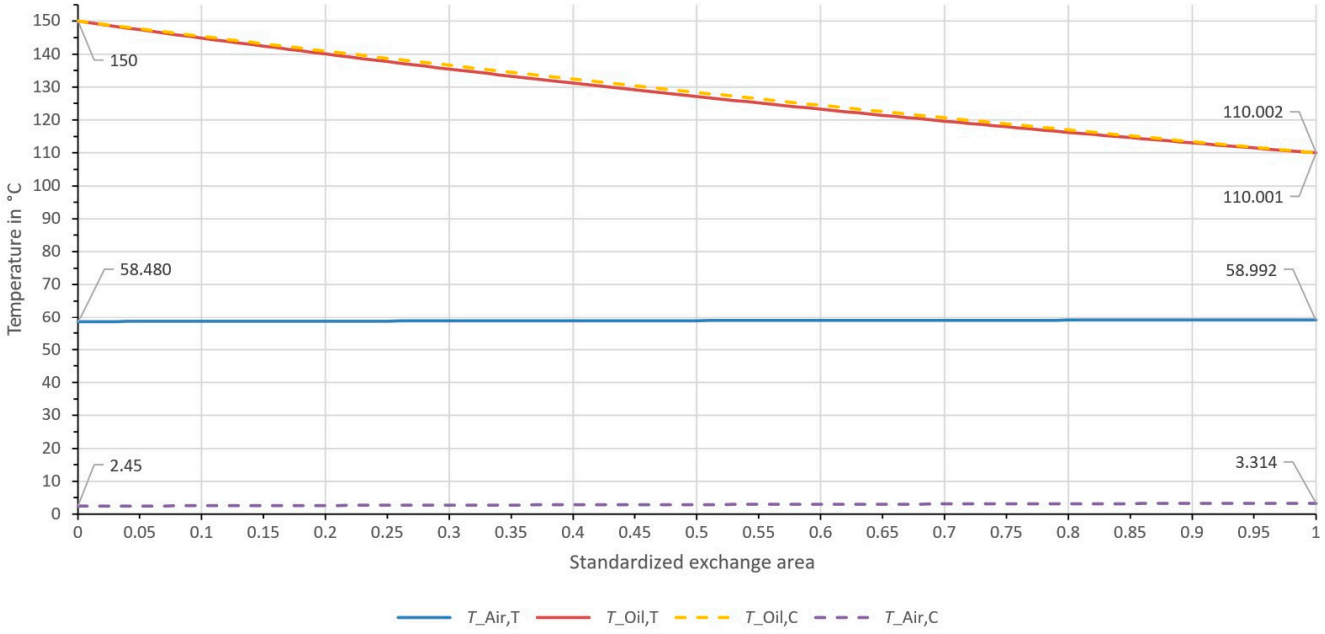


Figure 12. Temperature curve for take-off and cruise flight phases, with $A_{HX,min}$, P_V and $\dot{V}_{O,r}$.

The equation used only applies to direct-flow heat exchangers, where x serves as the normalized running variable for the surface. The equations used for this are (38) to (42).

$$T_O(x) = T_{O,out} - \frac{\dot{C}_{\mathrm{A}}}{\dot{C}_{\mathrm{A}} + \dot{C}_{\mathrm{O}}} \cdot \Delta T_{max} \cdot [1 - e^{(-k \cdot \mu \cdot A_{HX} \cdot x)}] \tag{38}$$

$$T_A(x) = T_{A,3} + \frac{\dot{C}_{\mathrm{O}}}{\dot{C}_{\mathrm{A}} + \dot{C}_{\mathrm{O}}} \cdot \Delta T_{max} \cdot [1 - e^{(-k \cdot \mu \cdot A_{HX} \cdot x)}] \tag{39}$$

The required heat capacity flow $\dot{C}_{\mathrm{O}}$ and $\dot{C}_{\mathrm{A}}$ can be calculated as follows:

$$\dot{C}_{\mathrm{O}} = \dot{V}_{\mathrm{O}} \cdot \rho_{O,m} \cdot cp_{O,m} \tag{40}$$

$$\dot{C}_{\mathrm{A}} = \dot{V}_{A} \cdot \rho_{A} \cdot cp_{A} \tag{41}$$

The difference between the parameters in the two flight phases must be taken into account. The parameter μ represents a constant that is defined as follows:

$$\mu = \frac{1}{\dot{C}_O} + \frac{1}{\dot{C}_A} \tag{42}$$

The existing heat exchanger surface area can be calculated using Equation (43). The surface area values are taken from Table 7. The variable n represents the number of guide vane blades. As can be seen in Figures 3 and 8a, the number of guide vane blades for a PW-1127G is $n = 48$.

$$A_{HX} = (A_{AS} + A_{AP}) \cdot n \tag{43}$$

The available surface area for heat transfer is, therefore, $A_{HX} = 8.855\text{m}^2$. A part of this surface is shown in blue for one guide vane in Figure 9.

4. Results

This section presents the thermal and aerodynamic performance of the proposed heat exchanger, assessing heat dissipation capability, temperature evolution, thrust gain, and specific fuel consumption improvement across relevant flight phases.

4.1. HX Comparison

By fully utilizing the entire available heat exchanger surface area A_{HX} and using the selected constant volumetric oil flow rate $\dot{V}_O = 204.96\,\text{l/min}$ for both flight phases, the following diagram (Figure 13) is obtained.

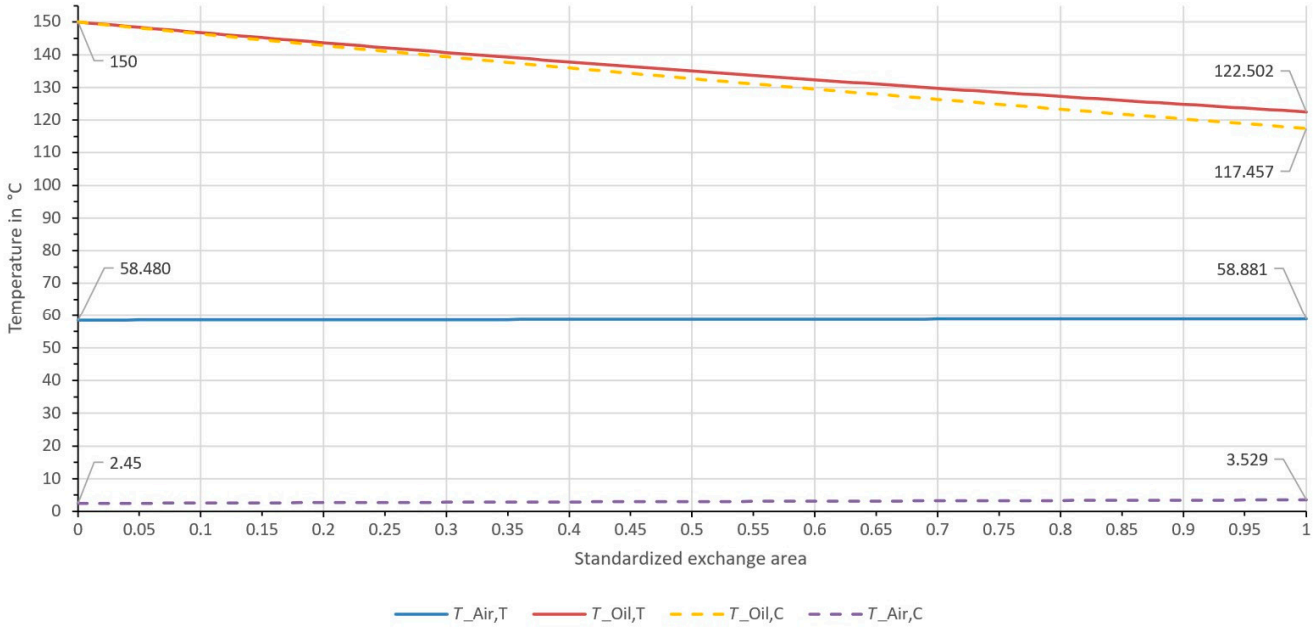


Figure 13. Temperature curve for take-off and cruise flight phases, with the values of $A_{HX,min}$, P_V and $\dot{V}_O$.

The larger oil flow rate reduces the $\Delta T_{O,m}$, while the gearbox heat energy remains constant. The lower $\Delta T_{O,m}$ also causes the $\Delta T_{m,\log}$ to decrease, which leads to an increase in the required surface area.

In both flight phases, the required final temperature of $T_{O,out} = 110\,^\circ\text{C}$ of the oil is not reached. A sufficient improvement can be achieved by slightly lowering the oil volume flow to $\dot{V}_{O,r}$.

Using the request oil mass flow $\dot{V}_{O,r}$ in Table 8 and making full use of the entire available heat exchanger surface area, the following diagram is now obtained.

During the cruise phase, the required surface area is smaller than the available surface area, which leads to excessively low oil temperatures. During the take-off phase, the available surface area is too small, which leads to too high oil temperatures of $T_{O,in} = 119.372$ °C. The air temperature will only rise up to $T_{A,3n} = 58.87$ °C, which corresponds to a $\Delta T = 0.392$ °C. To reduce the temperature during the take-off flight phase, a transient higher oil temperature would be advisable.

To maintain the required oil temperature under cruise operating conditions, the number of heat exchanger guide vanes can be reduced to 40 while still achieving the target air outlet temperature of $T_{A,3n,C} = 3.314$ °C. In this configuration, the total effective heat transfer surface area amounts to $A_{HX,40} = 7.379149$ m^2, which remains sufficient to ensure adequate thermal dissipation and stable system performance during cruise flight (see Figure 14).

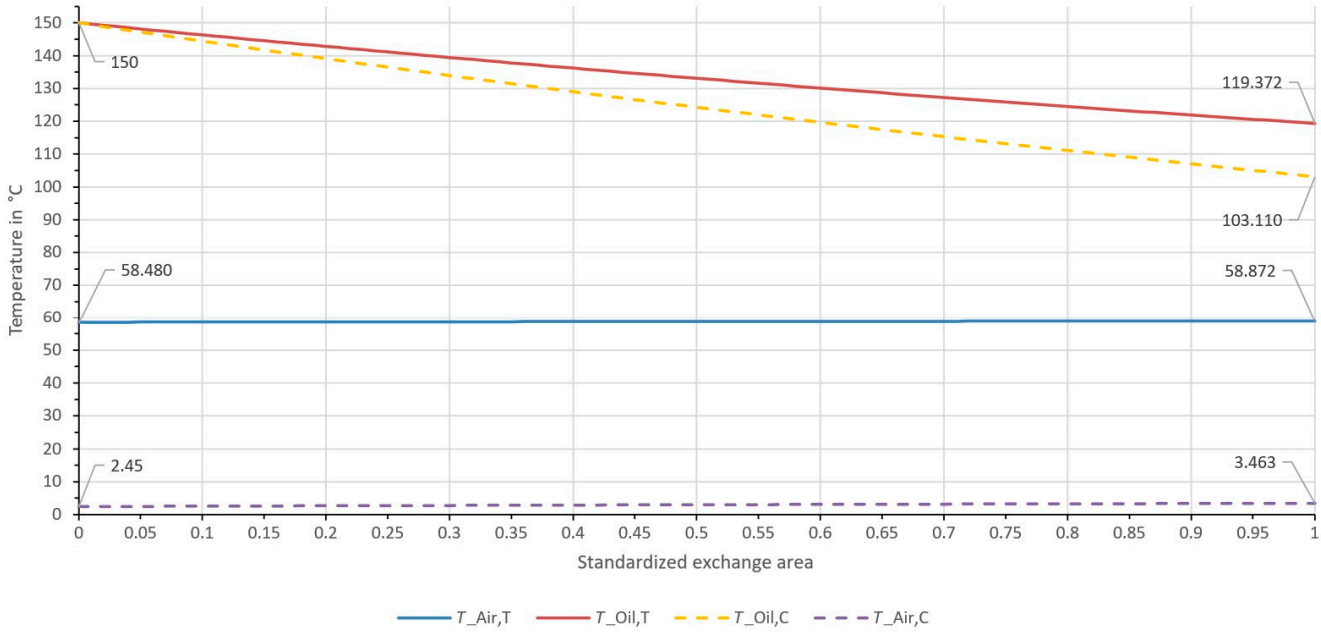


Figure 14. Temperature curve for take-off and cruise flight phases, with A_{HX} and $\dot{V}_O$, *for* P_V.

An additional approach would be to include additional power losses, such as $P_{V,AGB} = 35$kW losses, during the cruise phase. Since the maximum transferable power loss in cruise mode is $P_{V,max} = 208.021$ kW, it is possible to include additional power losses from the auxiliary gearbox. This would heat the air to $T_{A,3n} = 3.49$ °C. The total power loss would then increase to $P_{V,all} = 206.977$ kW. The results can be seen in Figure 15.

4.2. SFC Comparison

We performed a comparison of the specific fuel consumption SFC with and without the guide vane heat exchanger. The velocities and, therefore, the thrust forces can be calculated using Equations (2) to (6), as well as Tables 1 and 4. The results in Table 14 are based on the assumption that the surface area for heat transfer is sufficiently large, which is true in the cruise flight phase but not in the take-off flight phase, as already described in Section 4.1.

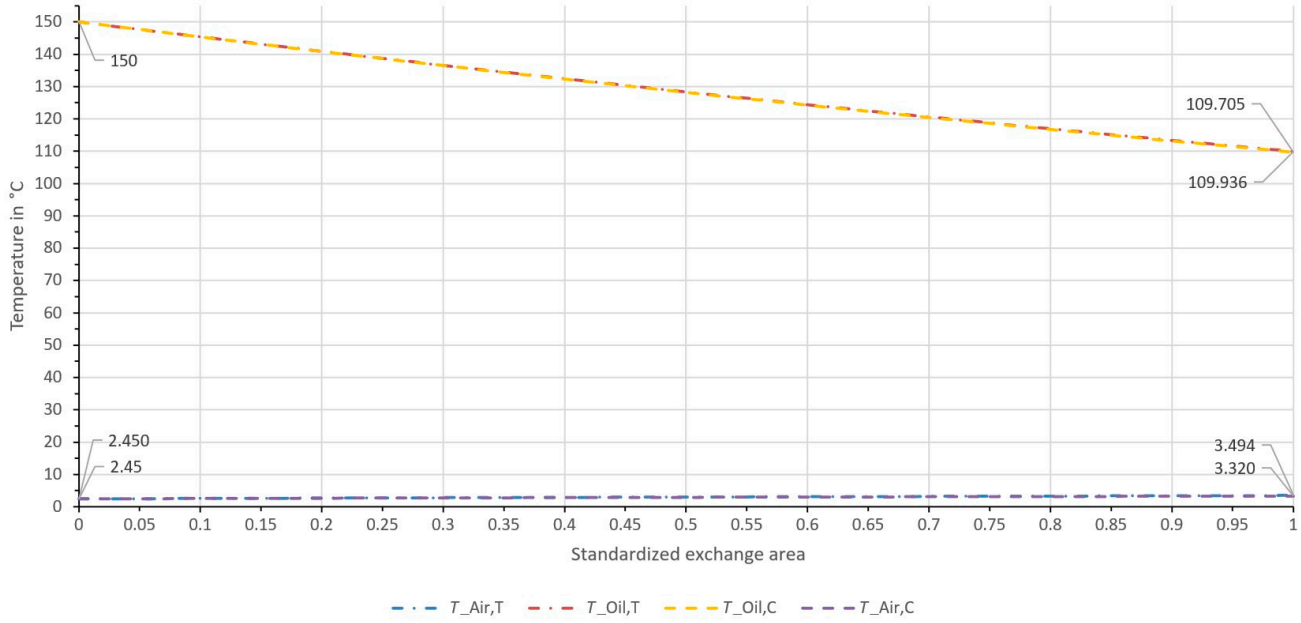


Figure 15. Temperature curve for cruise flight phases, with $A_{HX,40}$ and $P_{V,\,all}$.

Table 14. Thrust and efficiency results for $A_{HX,min}$ and P_V for take-off and cruise phases.

Parameter	Take-Off	Cruise
Jet velocity without HX c_4 $[\frac{m}{s}]$	247.522	329.279
New jet velocity with HX $c_{4,n}$ $[\frac{m}{s}]$	248.837	331.349
Thrust force without HX F_N [N]	111,175.249	19,023.117
Thrust force with HX $F_{N,HX}$ [N]	111,765.885	19,433.534
Thrust enhancement ΔF_N [N]	590.636	410.417
Thrust increase ε_F [%]	0.5312	2.1575
Specific fuel consumption $SFC_{T,n}$ $[\frac{g}{KN \cdot s}]$	6.9544	13.3538
SFC_T improvement ε_{SFC} [%]	0.489	1.907

In order to obtain the $SFC_{T,n}$, the thrust increase ΔF_N is added to the thrust F_N from the Gasturb calculation of Table 2; the fuel mass also originates from the gas turbine calculation. This results in an improved SFC_T due to the Junkers–Meredith Effect in the HX. The SFC_T improvement ε_{SFC} can be calculated with Equation (44):

$$\varepsilon_{SFC} = \frac{SFC_T - SFC_{T,n}}{SFC_T} \cdot 100\% \tag{44}$$

The SFC_T value of the Gasturb calculation is used as the basis for the ε_{SFC}. As can be seen in Table 14, the SFC improvement is more pronounced at higher Mach numbers, as in the cruise flight phase. Similarly, the thrust gain ε_F is lower in the take-off flight phase, which is due to the highest thrust demand.

Since only $A_{HX} = 8.855\ m^2$ is available instead of the required heat exchanger surface area $A_{HX,min} = 12.505\ m^2$ for the take-off flight phase, the air temperature increase ΔT_A is lower, as can be seen in Figure 13. During the take-off phase, the aircraft accelerates rapidly, causing a significant change in the Mach number from take-off $Ma_{A,0} = 0$ to the end of the flight phase $Ma_{A,0} = 0.25$. This directly affects the thrust increase, as can be seen in Equation (3). The resulting enhancement thrust ΔF_N and $SFC_{T,n}$ values are shown in Table 15 below.

Table 15. Thrust and efficiency results for A_{HX} and P_V at the start and end of the take-off phase.

Parameter	Take-Off ($Ma_0 = 0$)	Take-Off ($Ma_0 = 0.25$)
New jet velocity with HX $c_{4,n}$ $[\frac{m}{s}]$	248.792	263.381
Thrust force without HX F_N [N]	111,175.249	72,660.375
Thrust force with HX $F_{N,HX}$ [N]	111,745.673	79,783.497
Thrust enhancement ΔF_N[N]	570.424	7123.122
Thrust increase ε_F[%]	0.5131	6.4071
Specific fuel consumption $SFC_{T,n}[\frac{g}{KN \cdot s}]$	6.9544	6.5972
SFC_T improvement ε_{SFC} [%]	0.474	5.586

The greatest improvement in the SFC_T can be seen at the end of the take-off flight phase, with $\varepsilon_{SFC} = 5.586\%$. This value decreases until the cruise flight phase but can be increased by incorporating additional power losses, as shown in Figure 15. With the increased power loss $P_{V,all} = 206.977$ kW, the air temperature also rises, and therefore, the thrust increases, as can be seen in Table 16.

Table 16. Thrust and efficiency results for A_{HX} and $P_{V,all}$ for the cruise phase.

Parameter	Cruise ($P_{V,all}$)
New jet velocity with HX $c_{4,n}[\frac{m}{s}]$	331.455
Thrust force without HX F_N[N]	19,023.117
Thrust force with HX $F_{N,HX}$[N]	19,454.551
Thrust enhancement ΔF_N[N]	431.4334
Thrust increase ε_F[%]	2.2679
Specific fuel consumption $SFC_{C,n,all}[\frac{g}{KN \cdot s}]$	13.3407
SFC_Timprovement ε_{SFC} [%]	2.003

By dissipating the increased power loss from the power gearbox and auxiliary gearbox into the air in the bypass duct, the SFC_T improves by 2%. The existing heat exchanger surface area is utilized almost to its full capacity.

5. Discussion

5.1. Thermal Efficiency

Thermal efficiency η_{th} is mainly determined by the pressure ratio between the propulsor inlet and outlet, as seen in Equation (45) [4] (p.6):

$$\eta_{th} = 1 - \left(\frac{p_4}{p_0}\right)^{\frac{\varkappa-1}{\varkappa}} \tag{45}$$

An increase in the fan pressure ratio π_F (FPR) leads to a corresponding rise in the specific work imparted to the working fluid. As shown in Figure 16, the compression process performed by the fan elevates the flow enthalpy, necessitating mechanical energy input from the fan.

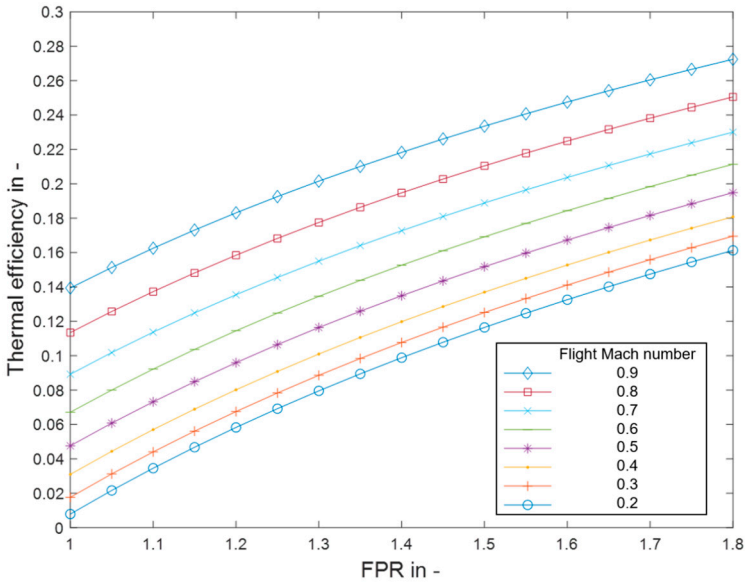


Figure 16. Thermal efficiency plotted over FPR for different flight speeds [4] (p.6).

Figure 16 shows the maximum limits of the Junkers–Meredith Effect at different Mach numbers and different FPRs. The FPR drastically increases the Junkers–Meredith Effect. The pressure difference caused by the FPR makes the guide vane the optimal position for utilizing the Junkers–Meredith Effect.

The parameters used for FPR and Mach numbers can be found in Table 3. Figure 16 shows that the thermal efficiency of the HX guide vanes in cruise mode is up to 20%. During the take-off phase, the efficiency increases continuously.

5.2. Take-Off Solutions

The thermal limitations of the gearbox require either an increase in the heat exchanger (HX) surface area or a higher allowable transient oil temperature to achieve sufficient heat dissipation during the take-off phase. Allowing a temporary rise in oil temperature while maintaining a constant HX surface area enables the dissipation of the full gearbox thermal load through the guide vane heat exchanger. An enlargement of the guide vane surface raises a modest pressure loss, which can negatively impact overall propulsive efficiency.

6. Conclusions

The proposed guide vane heat exchanger for the PW1127G-JM geared turbofan demonstrates a reduction of more than 5.5% in take-off thrust-specific fuel consumption SFC_T, corresponding to a thrust increase ε_{SFC} exceeding 6.4%. In cruise phase, the system achieves over 2% reduction in $SFC_{C,n}$ by using the Junkers–Meredith Effect. The cruise phase has a greater impact due to its relatively longer duration. It should be noted that the results refer to assumptions such as the simplified guide vane profile and gearbox oil.

To refine these findings, future work should employ fully coupled flow–thermal simulation models that account for turbulence–heat transfer interactions. Furthermore, increasing the chord length of the guide vane profile offers a promising design modification, as it substantially expands the effective heat transfer area and enables complete dissipation of transmission losses via the guide vane, including under peak load conditions during take-off. Additionally, a comparison between parallel-flow and counter-flow heat exchangers would be of interest, as these configurations exhibit distinct thermal performance characteristics and efficiency behaviors.

The key outcomes are as follows:

- Exploitation of the Junkers–Meredith Effect:

Gearbox thermal heat can be partially recovered into additional thrust while simultaneously reducing oil temperatures and improving propulsion efficiency.

- Compact design enabled shorter oil paths:

Due to the pronounced sweep of the guide vanes, their inner ends are located directly above the gearbox. Shorter oil lines reduce the required oil volume within the system.

- Large wetted surface:

With 48 guide vanes exposed to the bypass flow, a considerable surface area is available for heat transfer.

- High bypass mass flow:

The high airflow in the bypass duct compensates for the low thermal conductivity of air, resulting in a smaller required heat exchanger surface compared to conventional concepts.

- Future cooling capability:

This proposed design for a guide vane heat exchanger offers the possibility of adequately cooling future electric drives.

- Increase in power density of the geared turbofan:

The increase in thrust due to the Junkers–Meredith Effect increases both the gravimetric and volumetric power density.

Author Contributions: Conceptualization, G.B.H.-P.; methodology, G.B.H.-P.; software, G.B.H.-P.; validation, G.B.H.-P. and H.M.; formal analysis, G.B.H.-P.; investigation, G.B.H.-P.; resources, G.B.H.-P.; data curation, G.B.H.-P.; writing—original draft preparation, G.B.H.-P.; writing—review and editing, G.B.H.-P. and H.M.; visualization, G.B.H.-P.; supervision, H.M.; project administration, G.B.H.-P. All authors have read and agreed to the published version of the manuscript.

Funding: This research was funded by the Austrian Science Fund (FWF) 10.48436/87dh7-bm676.

Data Availability Statement: Data are available on request.

Acknowledgments: This research was funded in whole or in part by the Austrian Science Fund (FWF) 10.48436/87dh7-bm676. For open access purposes, the author has applied a CC BY public copyright license to any author accepted manuscript version arising from this submission.

Conflicts of Interest: The authors declare no conflicts of interest.

Abbreviations

The following abbreviations are used in this paper:

HX	Heat Exchanger
O	Oil
A	Air
C	Cruise
T	Take Off
FPR	Fan Pressure Ratio

References

1. European Commission. *The European Green Deal*; European Commission: Brussels, Belgium, 2019.
2. Statista. Passagierflugverkehr und Klimaschutz, Statista, 2024. Available online: https://de.statista.com/statistik/studie/id/70799/dokument/flugpassagierverkehr-und-klimaschutz/ (accessed on 30 July 2025).

3. International Civil Aviation Organization (ICAO). *Environmental Report 2022*; International Civil Aviation Organization (ICAO): Montreal, QC, Canada, 2022.
4. Gerl, B.; Ronvovsky-Bodisch, M.; Ferrari, N.; Berens, M. Fundamentals of Innovative Aircraft Heat Exchanger Integration for Hydrogen–Electric Propulsion. *Aerospace* **2025**, *12*, 320. [CrossRef]
5. Ronovsky-Bodisch, M.; Gerl, B.; Berens, M. Innovative aircraft heat exchanger integration for hydrogen-electric propulsion. *CEAS Aeronaut. J.* **2025**, 12. [CrossRef]
6. Kellermann, H. *Design of Thermal Management Systems for Future Aircraft*; TUM School of Engineering and Design, Technischen Universität München: Munich, Germany, 2024.
7. Meredith, F. *Cooling of Aircraft Engines*; Air Ministry: London, UK, 1935; p. 17.
8. Henrich, I. *Wie funktioniert ein Tubofan-Triebwerk?-Aufbau eines Triebwerks*; MTU Aero Engines: Munich, Germany, 2024. Available online: https://aeroreport.de/de/good-to-know/wie-funktioniert-ein-turbofan-triebwerk-aufbau-eines-triebwerk (accessed on 12 January 2026).
9. Bayindir, E.; Willinger, R. *Turbofantriebwerke mit Planetengetriebe für*; TU Wien, E302—Institut für Energietechnik und Thermodynamik: Vienna, Austria, 2025.
10. Peyfuß, G. *Entwicklungsperspektiven von Hochleistungsgetrieben in Turbofans*; TU Wien, E307-2 Institut für Konstrucktionswissenschaften und Produktentwicklung, Forschungsbereich Maschinenelemente und Luftfahrtgetriebe: Vienna, Austria, 2025.
11. Jafari, S.; Nikolaidis, T.; Van Heerden, A.S.J.; Lawson, C.P.; Bosak, D. Physicsbased thermal model for power gearboxes in geared turbofan engines. In Proceedings of the ASME Turbo Expo: Turbomachinery Technical Conference and Exposition, Virtual, 21–25 September 2020.
12. Pratt & Whitney. Pratt & Whitney Middletown Engine Center (17p1243-038). 2024. Available online: https://www.prattwhitney.com/en/newsroom/multimedia/middletown-engine-center (accessed on 25 January 2026).
13. Gasturb, 2025. Available online: https://www.gasturb.com/ (accessed on 25 January 2026).
14. EASA. *TYPE-CERTIFICATE PW1100G-JM Series Engines*; EASA: Cologne, Germany, 2012. Available online: https://www.easa.europa.eu/en/document-library/type-certificates/engine-cs-e/easaime093-pw1100g-jm-series-engines (accessed on 25 January 2026).
15. Hendricks, E.S.; Tong, M.T. *Performance and Weight Estimates for an Advanced Open Rotor Engine*; NASA, Glenn Research Center: Cleveland, OH, USA, 2012.
16. *ISO 5801*; Industrial Fans—Performance Testing Using Standardized Airways. International Organization for Standardization: Geneva, Switzerland, 1997.
17. Liebherr-Aerospace Lindenberg GmbH. *Lufo III "HDV-R-Test": Verifikation eines effizienten Schwerlastgetriebes hoher Drehzahl für Getriebefans*; Technical Report; Liebherr-Aerospace Lindenberg GmbH: Lindenberg, Germany, 2007.
18. The Engineering ToolBox. 2008. Available online: https://www.engineeringtoolbox.com/thermal-conductivity-liquids-d_1260.html (accessed on 20 November 2025).
19. Shell. *AeroShell Turbine Oil 500*; Shell: London, UK, 20 October 2025. Available online: https://www.shell-livedocs.com/data/published/en-GB/60360bb9-7856-4807-8470-ca54e950fd53.pdf?vid=6afd927172b04af68a090bb44a722c7b (accessed on 20 November 2025).
20. Rosen Metall-Service GmbH. *Werkstoffdatenblatt Titan Grade 5*; Rosen Metall-Service GmbH: Aachen-Eilendorf, Germany, 2025. Available online: https://rosen-metall.de/fileadmin/Werkstoffdatenblaetter/Sonderwerkstoffe/Werkstoffdatenblatt_TiG5.pdf (accessed on 20 November 2025).
21. Durmus, S.U.A. Numerical analysis of NACA 6409 and Eppler 423 airfoils. *Politek. Derg.* **2023**, *26*, 11. [CrossRef]
22. Verein Deutscher Ingenieure (VDI). *VDI-Wärmeatlas*; VDI-Gesellschaft Verfahrenstechnik und Chemieingenieurwesen, Ed.; Springer: Berlin/Heidelberg, Germany, 2013.
23. Lienhard, J.H., V.; Lienhard, J.H., IV. *A Heat Transfer Textbook*, 6th ed.; Phlogiston Press: Cambridge, MA, USA, 2024; p. 810.

Disclaimer/Publisher's Note: The statements, opinions and data contained in all publications are solely those of the individual author(s) and contributor(s) and not of MDPI and/or the editor(s). MDPI and/or the editor(s) disclaim responsibility for any injury to people or property resulting from any ideas, methods, instructions or products referred to in the content.